ARTICLE

MoS₂ Nanosheets Sensitized with Quantum Dots for Room-Temperature Gas Sensors

Jingyao Liu[1], Zhixiang Hu[1], Yuzhu Zhang[1], Hua-Yao Li[1], Naibo Gao[1], Zhilai Tian[1], Licheng Zhou[1], Baohui Zhang[1], Jiang Tang[1], Jianbing Zhang[1], Fei Yi[1], Huan Liu[1] ✉

✉ Huan Liu, huan@hust.edu.cn

[1] School of Optical and Electronic Information, Wuhan National Laboratory for Optoelectronics, Huazhong University of Science and Technology, 1037 Luoyu Road, Wuhan 430074, People's Republic of China

HIGHLIGHTS

- Highly sensitive and selective room-temperature NO₂ gas sensors by sensitizing MoS₂ nanosheets with PbS quantum dots were demonstrated. In this device architecture, the receptor and transduction function as well as the utility factor of semiconductor gas sensors could be enhanced simultaneously.

- The strategy of sensitizing 2D semiconductors with quantum dots as sensitive and selective receptors for gas molecules may offer a powerful new degree of freedom to the surface and interface engineering of semiconductor gas sensors.

ABSTRACT The Internet of things for environment monitoring requires high performance with low power-consumption gas sensors which could be easily integrated into large-scale sensor network. While semiconductor gas sensors have many advantages such as excellent sensitivity and low cost, their application is limited by their high operating temperature. Two-dimensional (2D) layered materials, typically molybdenum disulfide (MoS₂) nanosheets, are emerging as promising gas-sensing materials candidates owing to their abundant edge sites and high in-plane carrier mobility. This work aims to overcome the sluggish and weak response as well as incomplete recovery of MoS₂ gas sensors at room temperature by sensitizing MoS₂ nanosheets with PbS quantum dots (QDs). The huge amount of surface dangling bonds of QDs enables them to be ideal receptors for gas molecules.

The sensitized MoS₂ gas sensor exhibited fast and recoverable response when operated at room temperature, and the limit of NO₂ detection was estimated to be 94 ppb. The strategy of sensitizing 2D nanosheets with sensitive QD receptors may enhance receptor and transducer functions as well as the utility factor that determine the sensor performance, offering a powerful new degree of freedom to the surface and interface engineering of semiconductor gas sensors.

KEYWORDS Gas sensor; Room temperature; Molybdenum disulfide; Quantum dot; Nitrogen dioxide
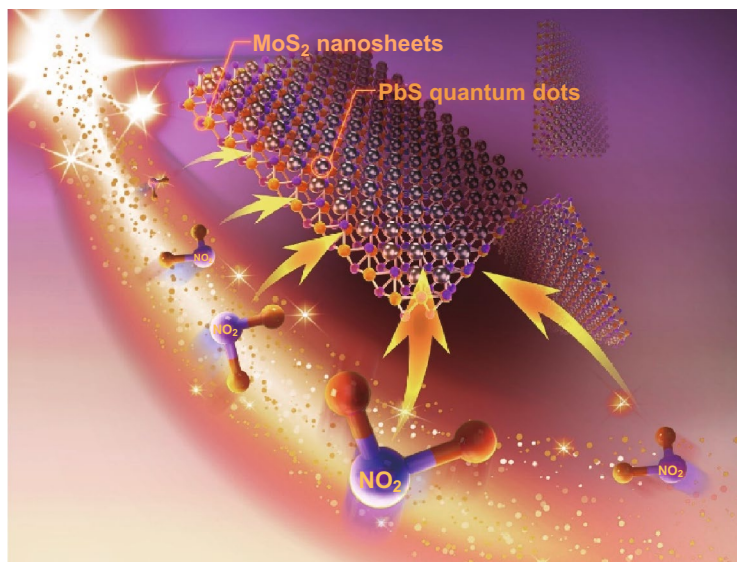
1 Introduction

Hazardous air pollutants have become a serious problem for the ecosystem and public health [1, 2]. Nitrogen dioxide (NO_2) primarily gets in the air from the burning of fuel. Exposure to NO_2 may potentially increase susceptibility to respiratory infections, and a 5-min emergency exposure limit of 35 ppm NO_2 exposure has been proposed by the American Industrial Hygiene Association [1, 3]. The large-scale networking of gas sensors for achieving online NO_2 monitoring requires the power consumption of the sensors to be lower. While semiconductor gas sensor have been widely used in home alarm system owing to their high sensitivity, simple operation, and low cost [4–6], their scale-up application in environmental internet has not been achieved due to the limitation of high operating temperature (typically above 300 °C) which raises the power consumption. The high operating temperature of semiconductor gas sensors also sets a limit to their integrability with CMOS technology or flexible electronic system. Thereby, novel nanostructured materials [7–10] with the potentials for room-temperature gas sensors have become a hot research topic.

MoS_2 is a well-known 2D graphene-like transition metal dichalcogenides (TMDs). With relatively high carrier mobility, large surface-to-volume ratio, and abundant edge sites which can provide active adsorption sites for gas molecules [11–14], MoS_2 has been demonstrated as one of the promising materials candidates for room-temperature NO_2 gas sensors. Liu et al. [13] reported CVD growth of monolayer MoS_2 for room-temperature detection of NO_2 with a response time of several minutes without a full recovery to the initial state. Cho et al. [15] demonstrated a charge-transfer-based sensitive NO_2 gas sensor by CVD-synthesized atomic-layered MoS_2, with a sensitivity of 220% and a long time (more than 30 min) to recovery. Similarly, chemical exfoliated MoS_2 prepared by Jung et al. had an incompletable recovery to NO_2 at room temperature [16]. Kumar et al. fabricated a high-performance NO_2 sensor based on MoS_2 with abundant active edge sites. When operated at 60 °C, it had a fast response (16 s) with complete recovery (172 s) with a relative response of 18.1% to 5 ppm NO_2 [17]. As an alternative strategy, UV light irradiation or gate effect was employed to improve sensitivity toward NO_2 of MoS_2 sensor [18–21]. Pham et al.

[18] employed LED illumination to improve sensitivity of CVD grown single-layer MoS_2, achieving sub-ppb limit of NO_2 gas detection. However, the comparatively high sensitivity and fast response/recovery kinetics at room temperature were not simultaneously obtained for pristine MoS_2 gas sensors. They suffer from the trade-off between receptor and transducer function. For semiconductor gas sensors, the structural defects are always necessary for gas molecule reception and, on the contrary, may decrease the electronic transduction.

Recently, MoS_2-based nanocomposites or hybrids through surface modification with noble metals [11], architecture design of hetero-nanostructures with metal oxide nanoparticles [22, 23], and functionalization with other 2D-layered materials such as graphene [24–28] have been demonstrated with improved sensitivity and fast response/recovery kinetics. Motivated by this strategy, we proposed to improve the room-temperature response and recovery by sensitizing MoS_2 nanosheets with quantum dots (QDs), a highly tunable zero-dimensional (0D) nanomaterial with size-dependent bandgap and excellent solution processability [29–35]. The huge amount of surface dangling bonds of QDs makes them sensitive receptors for gas molecules. Herein, the PbS QDs-sensitized MoS_2 nanosheets were obtained via a two-step solution process. The sensor had an excellent response of 6.15, to 10 ppm NO_2 at room temperature, almost five times greater than that of pristine MoS_2 nanosheets. The sensing mechanism was attributed to the enhanced receptor and transducer functions as well as the utility factor which determine the performance of semiconductor gas sensors.

2 Experimental

2.1 Preparation of MoS_2 Nanosheets

In a typical hydrothermal synthesis of MoS_2 nanosheets [36], as shown in Fig. 1a, 1 mmol hexaammonium heptamolybdate tetrahydrate (($NH_4)_6Mo_7O_{24} \cdot 4H_2O$) and 14 mmol thiourea were dissolved into 35 mL of deionized water under stirring for several minutes to form a homogeneous solution. The mixed solution was transferred into a 50-mL Teflon-lined stainless steel autoclave to react at 220 °C for 18 h and then naturally cooled down to room
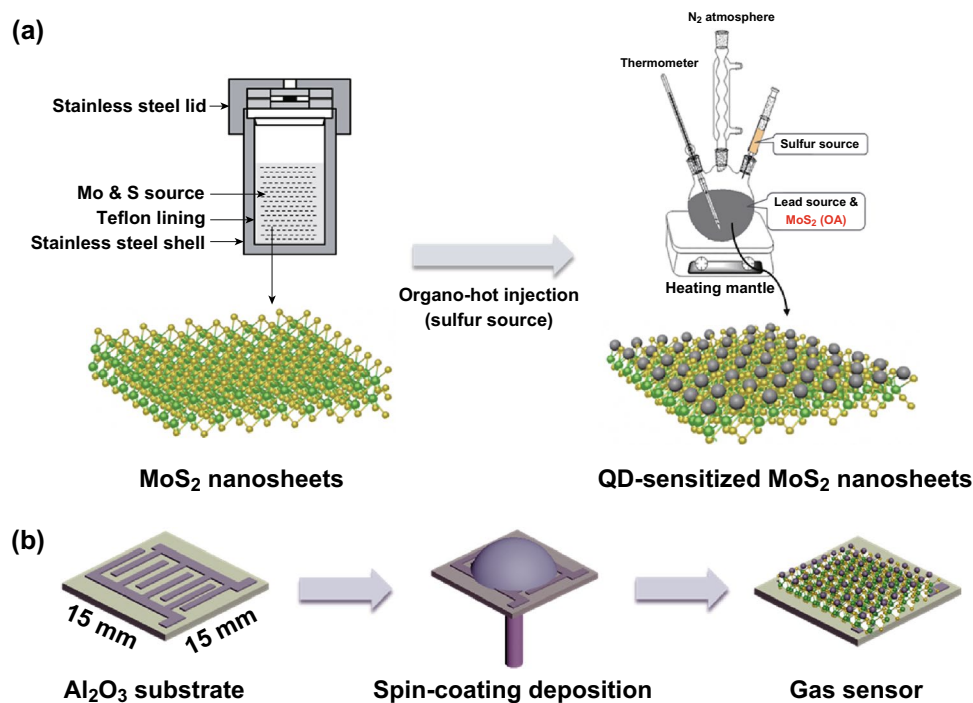
Fig. 1 Schematic illustration of **a** formation of the MoS_2 nanosheets and QD-sensitized MoS_2 nanosheets and **b** fabricated process diagram of the sensitized structure-based gas sensors

temperature. The final product was rinsed with deionized water and absolute ethanol several times to remove any possible ions. After drying at 70 °C for 6 h, black MoS_2 nanosheet powder was obtained.

2.2 Synthesis of MoS_2 Nanosheets Sensitized with QDs

Figure 1a shows the synthesis of MoS_2 nanosheets sensitized with PbS QDs. Organo-hot injection method has always been proven as an effective method for QD synthesis [37–39]. First, the as-prepared MoS_2 powders (20 mg) were dissolved in 4 mL of oleic acid (OA). Ultrasonic dispersion was conducted for 30 min to ensure the black powder was completely dispersed in the solution. PbO (2 mmol), OA (2 mmol), 1-octadecene (ODE) (20 mL), and as-prepared MoS_2 (OA) solution (530 μL) were all mixed in a three-neck flask and heated to 90 °C under a vacuum for 6 h. Then, the reaction temperature was raised to 120 °C and 0.33 mmol bis(trimethylsilyl) sulfide (TMS) mixed with ODE (10 mL) was rapidly injected under an inert atmosphere. The reaction lasted for 30 s, and the mixture was then transferred to cold water bath for rapid cooling to room temperature. The

nucleation and growth of QDs anchoring in the surface of MoS_2 nanosheets occurred in this process. The product was precipitated by acetone and re-dispersed in toluene several times to prepare PbS–MoS_2 solution for device fabrication.

2.3 Sensor Fabrication

The layer-by-layer spin-coating deposition technique of the sensitized MoS_2-based thin film was carried out in ambient air at room temperature (a schematic illustration can be seen in Fig. 1b). Alumina ceramic substrates ($15 \times 15 \times 0.8$ mm³) prepatterned with a pair of interdigital Ag electrode (the spacing and width are 5 mm) were prepared via screen printing. Then 70 μL of PbS–MoS_2 solution was dropped onto the substrate, which was then spun at 2350 rpm for 30 s. Next, four drops of $NaNO_2$ diluted in methanol (10 mg mL⁻¹) were added dropwise to the film for ligand exchange, with a wait time of 45 s, and spun dry at 2500 rpm for 30 s, followed by repeating the $NaNO_2$ treatment twice. Finally, the film was washed by methanol flush and then spun dry three times to obtain 3-layers thin-film device. The film deposition process was

repeated three times. For comparison, the pristine MoS_2 nanosheet device was prepared according to the following steps. First, the prepared substrates were placed in a hot-plate with a heating temperature of 135 °C. Next, a drop of MoS_2 ethanol solution was deposited dropwise onto the thermal substrate and naturally dried for a few seconds, followed by repeating the process twice. Finally, the fabricated MoS_2 sensor was maintained under the thermal treatment for 20 min.

2.4 Characterization and Measurements

A field emission scanning electron microscope (FE-SEM, GeminiSEM 300, Zeiss, Oberkochen, Germany) equipped with an energy-dispersive X-ray spectrometer (EDS, X-MAX, Oxford, UK) was used to obtain SEM images and elemental mapping data. Transmission electron microscopy (TEM) images were recorded with a Tecnai G2 20 microscope operating at an accelerating voltage of 200 kV. X-ray diffraction (XRD) measurements were obtained using a diffractometer (Empyrean, PANalytical B. V., Netherlands) with Cu Kα radiation in the 2θ range of 10–70 °C. An energy-dispersive X-ray spectrometer (EDS) was performed on a XL 30 ESEM FEG. X-ray photoelectron spectroscope (XPS) measurements were using by an AXIS-ULTRA DLD-600 W with an Al source, and C 1s peak at 284.5 eV is used as reference. Similarly, ultraviolet photoelectron spectroscopy (UPS) measurement was also performed by using the same system with a He-Iα 21.22 eV UV light. Work functions were measured by a KP 020 K probe (KP Technology, Wick, Scotland). UV–Vis–NIR absorption spectra were measured using a PerkinElmer Lambda 950 UV–Vis–NIR spectrophotometer.

The NO_2 sensing measurements were carried out by a computer-connected source meter system (Model Keithley 2450/6487, Keithley Instruments, USA) under static conditions controlled with the relative humidity (RH) being 19–85% at room temperature (sensor setup details as shown in Fig. S1). The sensor response was defined as the ratio of R_a to R_g, where R_a is the baseline resistance in the ambient atmosphere and R_g is the resistance of the sensor device in the presence of NO_2 gas. The response time (T_{90}) and the recovery time (T_{10}) were defined as the time taken by the sensor response to reach 90% of its maximum value upon exposure to NO_2 gas and drop to within 10% of its original baseline value after removal of gas.

3 Results and Discussion

3.1 Structural Properties of MoS$_2$ Nanosheets and QD-Sensitized MoS$_2$ Nanosheets

The morphology of the MoS_2 and QD-sensitized MoS_2 nanosheets was characterized with SEM and TEM, respectively. Figure 2a displays a low-magnification TEM image of MoS_2 nanosheets revealing the ultrathin nanosheet morphology with slightly assembly character. Further, more lattice fringes were clearly indicated from high-magnification TEM image (Fig. 2b), revealing the labeled lattice spacing of 0.625 nm, which was in a good agreement with the (002) lattice plane with MoS_2 nanosheets. The abundant MoS_2 nanosheets layers provide large quantities of edge sites, which may beneficial for gas molecules absorption. Moreover, Fig. S2 shows an SEM image of the as-prepared MoS_2 nanosheets distributed on the alumina ceramic substrate, and the observable flowerlike MoS_2 nanosheets were uniformly assembled by a mass of bent flakes. Similarly, TEM images of different magnifications in Fig. 2c, d used to observe more detailed microstructure information of the QD-sensitized MoS_2 nanosheets. A large amount of QDs formed on the edge sites of the MoS_2 nanosheets as demonstrated in Fig. 2c. This could be attributed to the edge area defects, which provide more active sites for the nucleation of PbS QDs. Pb atoms can fill the vacancy on the MoS_2 surface, which may weaken the MoS_2 defects [40]. Equally important is that the MoS_2 surface might be spontaneously functionalized with the excessive OA molecules in the reaction process, and then the strong hydrophobic interaction [41, 42] of the OA ligands on both the QDs and MoS_2 surfaces leading to the noncovalent binding of QDs to MoS_2. However, the detailed mechanisms regarding how the OA ligands or molecules take part in the synthesis of MoS_2 nanosheets sensitized with QDs need further investigation. The efficient attachment and coverage of the QDs onto the MoS_2 nanosheets are further indicated by the high-resolution TEM image in Fig. 2d. Well-crystallized QDs with diameters of approximately 3.26 nm were uniformly separated on the surface of the MoS_2 nanosheets.
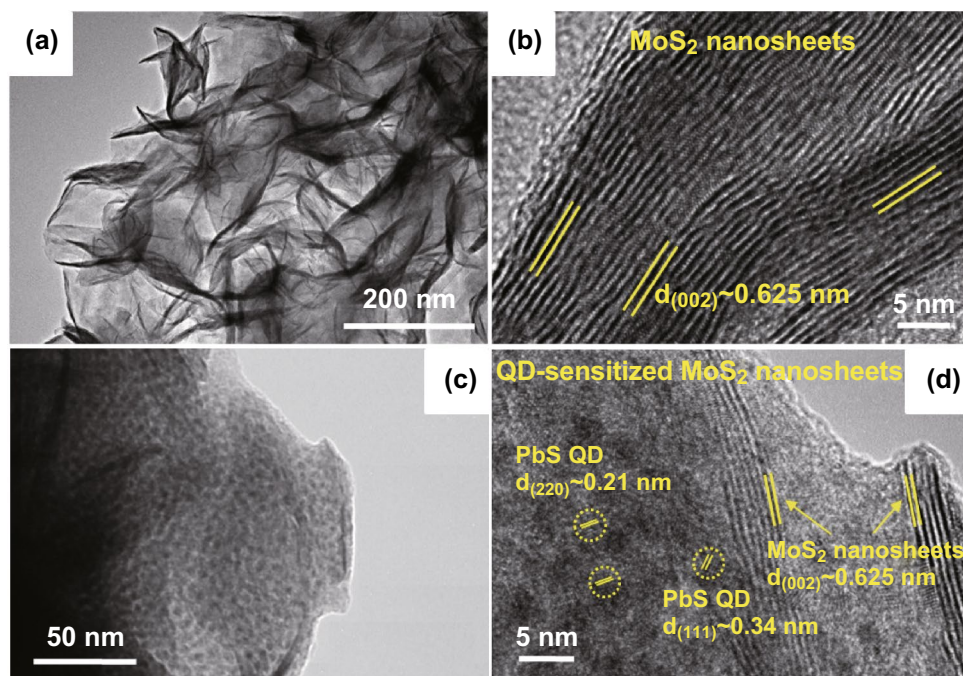
Fig. 2 Morphology of the MoS_2 nanosheets and QD-sensitized MoS_2 nanosheets: **a**, **b** TEM images of the flowerlike MoS_2 nanosheets and **c**, **d** QD-sensitized MoS_2 nanosheets at different magnifications, showing a lattice space of 0.625 nm corresponding to the (002) lattice plane of MoS_2, and 0.21, 0.34 nm corresponding to the (220), (111) lattice planes of PbS, respectively

The lattice spacings of these spherically shaped QDs were 0.21 and 0.34 nm, corresponding to the (220) and (111) lattice planes of PbS, respectively. The edges of the MoS_2 nanosheets were not continuous, probably because some defects were generated in the synthesis processes. The typical elemental mapping data were characterized by EDS, as shown in Fig. S3a–e, which also confirmed the even distribution of the Pb and Mo element in the final actual

device, revealing the formation of well-distributed PbS QDs in the MoS_2 nanosheets.

To further confirm the structural information of the MoS_2 and QD-sensitized MoS_2, the XRD patterns of the samples are shown in Fig. 3. It indicates that the four sharp diffraction peaks centered at approximately $2\theta = 13.9°$, 33.4°, 39.4°, and 58.9° of the powder MoS_2 could be well-indexed, respectively, to the (002), (100) + (101), (103), and
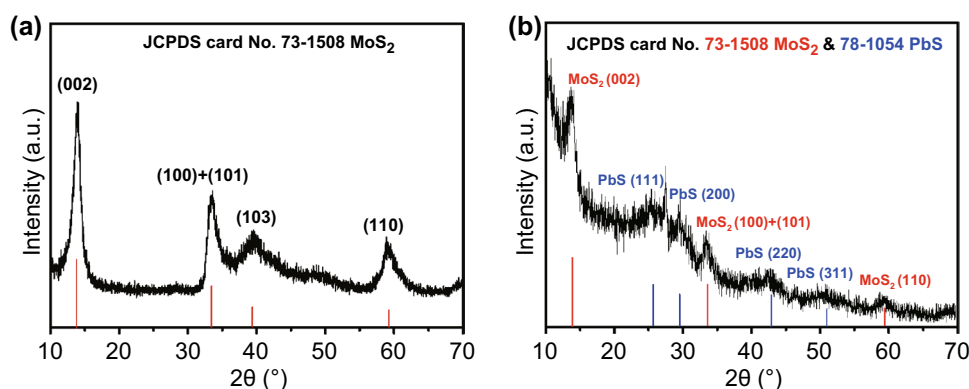

Fig. 3 XRD patterns of **a** MoS_2 nanosheet and **b** QD-sensitized MoS_2 nanosheets

(110) planes of the hexagonal phase MoS$_2$ (JCPDS card No. 73-1508). The strong (002) peak at $2\theta = 13.9°$ with a d-spacing of approximately 0.625 nm corresponded to a well-stacked layered structure along the c axis as well as the TEM results. Compared to the pristine MoS$_2$, the XRD patterns of the sensitized structure in Fig. 3b contained some extra peaks other than the main characteristic peaks of MoS$_2$. The peaks at approximately $2\theta = 25.3°$, 29.6°, 42.8°, and 51.4° were not only well matched with the (111), (200), (220), and (311) planes of cubic PbS (JCPDS card No. 78-1054), which indicated the successful growth of PbS QDs on the surface of MoS$_2$ nanosheet, but also consistent with the TEM characteristics presented in Fig. 2d. The significantly broadened peak that appeared on PbS could possibly be attributed to the quantum size feature of the QDs, according to the Debye–Scherrer equation.

The surface elements and chemical states of the sensitized MoS$_2$-based film were characterized by X-ray photoelectron spectroscopy (XPS) in the supporting information. As expected, Pb, Mo, and S were detected on the film, which was consistent with the EDS results. Figure S4a–c shows the high-resolution XPS spectra of Pb 4f, S 2p, and Mo 3d, respectively. Two peaks located at 142.7 and 137.8 eV correspond to the 4f$_{5/2}$ and 4f$_{7/2}$ of the Pb^{2+} state exhibited in Fig. S4a. Most of the Mo signal is from its Mo^{4+} state at the peak positions around 228.5 and 229.2 eV, mainly corresponding to Mo^{4+} 3d$_{5/2}$ (Fig. S4c). Two dominant S 2p peaks were observed around 161.5 and 162.2 eV (Fig. S4b), accompanied by a slightly flat peak at 163.8 eV, which were assigned to the divalent sulfide ions (S^{2-}) of the MoS$_2$ and PbS.

3.2 NO$_2$ Gas-Sensing Properties

The NO$_2$-sensing performance was measured using a home-made computer-connected source meter system under room temperature. We performed repeatability test for the both devices at the same time and measured the relative response to six and four successive cycles toward 10 ppm NO$_2$ for pristine MoS$_2$ nanosheets and the sensitized MoS$_2$ gas sensors, respectively (Fig. S5a). The pristine MoS$_2$ sensor showed the complete recovery at room temperature without any extra stimulus such as optical or thermal source; however, the completed response/recovery cycle required a slightly time. After sensitization by the PbS QDs, the sensitized MoS$_2$ sensor exhibited an obviously enhanced response to the same concentration of NO$_2$ gas, also with a fast response/recovery time and excellent reversibility. Transient resistance characteristic of MoS$_2$ nanosheets and the sensitized MoS$_2$ gas sensors to 10 ppm NO$_2$ is shown in Fig. S5b, exhibiting p-type gas-sensing behavior for both sensors. The improved performance can be attributed to the excellent access of gas molecules adsorption by the PbS QDs as NO$_2$ receptors, as well as the favorable 0D-2D interface for charge transfer, which will be discussed in detail later. Three kinds of theoretical Mo to Pb molar ratio (2%, 5%, and 8%) were used in the precursor solutions during the synthesis, and we found that sensor response was much higher by a medium molar ratio of 5% (Fig. S6). Thus, we used this optimal molar ratio to sensor fabrication in this work. The representative time-resolved response and recovery curves of the pristine MoS$_2$ and the sensitized MoS$_2$ gas sensor were illustrated in more detail in Fig. 4a, b. In general, many defects may occur in the surface of MoS$_2$, which can lead to a strong chemisorption between MoS$_2$ and gas molecules, so that NO$_2$ or other gases such as O$_2$ are difficult to desorb from the MoS$_2$ [43], resulting in a weakened recovery kinetics, as shown in Fig. 4a. The sensitized MoS$_2$ sensor exhibited a superior performance not only with an excellent response of 6.15 to 10 ppm NO$_2$, which was almost five times greater than the pristine MoS$_2$ device, but also with an outstanding response/recovery ability, with the time improving from 50/233 to 15/62 s, respectively.

To further investigate the NO$_2$-sensing properties of the sensors, the dynamic response curves were recorded with the NO$_2$ concentration of 1, 2, 5, 10, and 20 ppm, respectively, shown in Fig. 4c. Both devices showed recoverable response under room temperature, and the response values gradually increased with the increasing NO$_2$ gas concentration. Obviously, the device based on MoS$_2$ nanosheets sensitized with QDs was more sensitive than the pristine MoS$_2$ for NO$_2$ gas detection and indicated potential for a lower limit of detection (*LOD*). The pristine MoS$_2$ had less of a response when exposed to 1 ppm NO$_2$, while the sensitized MoS$_2$ sensor still performed 2.30 toward the same concentration with a rapid response/recovery rate, which even better than the measurement to 20 ppm of pristine MoS$_2$ device (details are shown in Fig. S7). Owing to this improvement, the theoretical *LOD* for NO$_2$ was calculated to be 174 and 94 ppb in the case of pristine MoS$_2$ and QD-sensitized MoS$_2$, respectively (calculation details in Fig. S8). However, the measurement error of the *LOD* for both sensors is mainly from accuracy
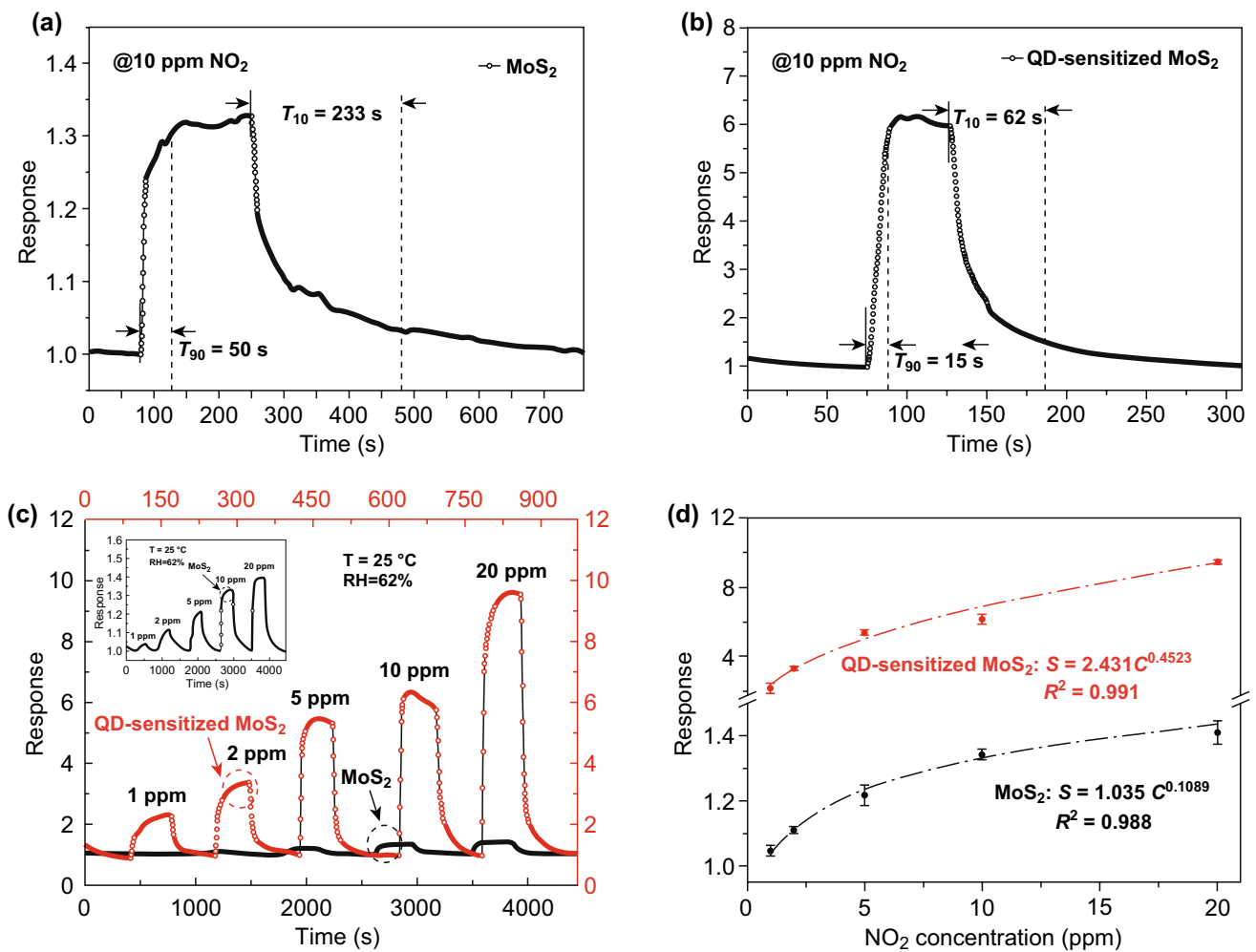
Fig. 4 Time-resolved response and recovery curves of **a** MoS$_2$ nanosheets and **b** the sensitized MoS$_2$ gas sensors exposed to 10 ppm NO$_2$ at room temperature. **c** Transient relative response of both sensors toward different NO$_2$ concentrations. **d** The relative response versus the NO$_2$ concentration illustration of the MoS$_2$ and the sensitized MoS$_2$ sensors

of gas concentration and errors in test results. The dependence of the sensor response on gas concentrations range from 1 to 20 ppm is also analyzed in Fig. 4d. The fitting equation between the response value (*S*) and NO$_2$ concentration (*C*) can be illustrated as a power law relationship, and the exponent was estimated to be 0.1089 together with a coefficient of determination (R^2) value of 0.988 for the MoS$_2$ sensor, while the values were 0.4523 and 0.991 for the sensitized MoS$_2$ sensor. Importantly, the theoretical analysis of the relationship between the response values and gas concentrations was significant for the gas sensor, which will facilitate the determination of gas concentrations in practical applications. Selectivity is considered as an important

parameter for gas sensors, and we compared the response of the sensitized MoS$_2$ gas sensors toward several gases in our lab. As shown in Fig. 5, the sensors exhibited high response to 10 ppm NO$_2$ gas and negligible response to 10 ppm H$_2$, SO$_2$, NH$_3$ and 200 ppm C$_2$H$_5$OH vapor, respectively, at room temperature. The inset showed the dynamic response curves upon gas exposure and release of the intervening gases, respectively. We also investigated the NO$_2$-sensing performance of the sensitized MoS$_2$ sensors in the range of RH of 19%, 29%, 48%, 65%, and 85%. The sensor response toward 10 ppm NO$_2$ had a tendency to grow over the RH gradually increased (shown in Fig. S9a). While the functional relationship between relative humidity and response could be further
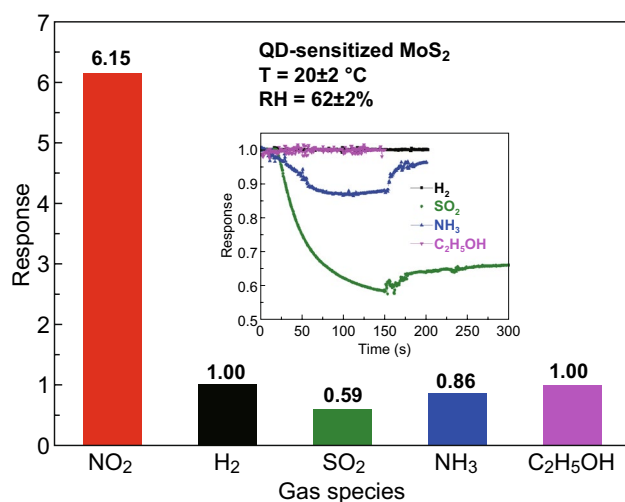
Fig. 5 Selectivity of QD-sensitized MoS$_2$ gas sensors toward different gases: 10 ppm NO$_2$, H$_2$, SO$_2$, NH$_3$ and 200 ppm C$_2$H$_5$OH

defined clearly, we can use humidity compensation methods to make our sensors satisfy the practical application under environment with a wider range of the RH. More details are shown in Fig. S9b about the real-time sensing curves toward 10 ppm NO$_2$ at different RH based on the sensitized MoS$_2$ gas sensors, revealing fast response/recovery kinetics under any RH environments. For this specific investigation, the RH value was intentionally controlled at certain values with

an accuracy of 2%. The average sensitivity to 10 ppm NO$_2$ under RH ~ 65% was 6.19, which was close to the average sensitivity of 6.14 under RH ~ 62% (Fig. 4d). Therefore, the RH ranged from 62 to 65% was within the error range. Under high RH environments, we suspected that water molecules preadsorbed on the surface of the sensitized MoS$_2$, dissociating into OH$^-$ and H$^+$ to form hydroxyl groups. Hydroxyl groups as an electron donor lead to increase in resistance of the materials [44]. NO$_2$ has strong adsorption properties compared with the physical adsorption of water molecules. When NO$_2$ injected, they could kick out the physical adsorption of water molecules and cause a further decrease in resistance, thus achieving a higher response. Actually, it is reported that the hydroxyl groups could improve the NO$_2$-sensing performance in recent study [35, 45–47].

Compared to other MoS$_2$-based NO$_2$ sensors (Table 1), our MoS$_2$ nanosheets-based sensor only maintained a general level at room-temperature (RT) operation; however, under the same conditions, the sensitized MoS$_2$ sensor had a superior performance with no thermal treatment or UV illumination [21, 48]. Compared to the most MoS$_2$-based gas sensors in the current published papers, the sensitized MoS$_2$ gas sensor exhibited an excellent response from 6.15 to 10 ppm NO$_2$ at room temperature, accompanied by a rapid response/recovery time of 15/62 s, indicating high sensitivity

Table 1 NO$_2$-sensing performance of MoS$_2$-based sensors

Materials	Method	Work temperature (°C)	Concentration (ppm)	Response (%)	T_{90}/T_{10} (s)	References
Few-layer MoS$_2$	Mechanically exfoliating	RT	100	60	180/600	[12]
Monolayer MoS$_2$	CVD	RT	0.4	80	~420/-(incomplete)	[13]
Few-layer MoS$_2$	CVD	RT	10	60	~60/~1000	[14]
Atomic-layered MoS$_2$	CVD	RT	1.2	150	~60/~1800	[15]
MoS$_2$ nanowires	CVD	60	5	18.1	16/172	[17]
Single-layer MoS$_2$	CVD	RT with LED light	0.1	~6	~500/~1	[18]
Multilayer MoS$_2$	Mechanically exfoliating	RT with gate effect	100	4	~60/~60	[19]
Multilayer MoS$_2$	CVD	RT with UV light	100	35	29/350	[48]
Mixed MoS$_2$ flakes	CVD	RT with UV light	10	21.78	6.09/146.49	[21]
SnO$_2$ NC-MoS$_2$ NS	Chemical exfoliation	RT	10	28	400/180	[22]
ZnO NPs/MoS$_2$ NSs	Wet chemical method	RT	5	3050	40/~600	[23]
MoS$_2$-RGO	Liquid exfoliation and hydrothermal	160	3	129	8/20	[25]
WS$_2$ functionalized MoS$_2$	Hydrothermal process	RT	50	26.12	1.6/< 30	[26]
MoS$_2$ nanosheets	Hydrothermal	RT	10	133	50/233	This work
MoS$_2$ nanosheets sensitized with QDs	Hydrothermal and organo-hot injection	RT	10	615	15/62	This work

and outstanding recovery ability. In addition, as shown in Fig. S9c, long-term stability test of the sensitized MoS_2 sensor upon 10 ppm NO_2 was consistent with the effect of relative humidity on the sensing performance. Furthermore, QD-sensitized MoS_2 nanosheets with excellent solution processability are particularly attractive for next-generation gas sensors compatible with silicon-based or flexible substrates.

3.3 Gas-Sensing Mechanisms

As previously noted, the gas sensor based on MoS_2 nanosheets sensitized with QD had a good NO_2-sensing performance at room temperature, which was quite possible for the combinational effects between the PbS QDs and MoS_2 nanosheets. Therefore, we proposed three basic factors of receptor function, transducer function and utility [49], as well as an interface energy band diagram to investigate the sensing mechanism of QD-sensitized MoS_2 nanosheets. As illustrated in Fig. 6a, PbS QDs always exhibited p-type conduction behavior in air atmosphere because of physisorbed O_2 molecules, which consumed electrons and introduced lots of holes as well. When exposed to NO_2 gas, according to our previous research [32, 34, 35], due to the strong binding energy compared to O_2, NO_2 kicks out the originally physisorbed O_2 molecules and binds to Pb^{2+}

through O, introducing more charge-transfer-driven p-type doping and developing a hole concentration in the p-type PbS QDs. For pristine p-type MoS_2 nanosheets, the defects mainly on the edge sites of the MoS_2 acted as active sites for NO_2 molecules, and these defects dominated process contributing to the poor response, slow rates of response, or even incomplete recovery due to high energy binding sites [50], especially operation at room temperature without any illumination. Thus, the inevitable receptor–transducer function [51] conflict cannot be well addressed in the pristine MoS_2-based gas sensor. After sensitization with QDs (illustrated in Fig. 6b), most of the high energy binding sites on the surface of MoS_2 were occupied by the highly active QD receptors which had larger surface-to-volume ratio as well as abundant surface defects (mainly from dangling bonds, surface Pb sites, sulfur vacancies, etc.) capable of active interaction with NO_2 gas molecules adsorption, contributing to a marked enhancement in the response. Furthermore, the adsorption energies of NO_2 on the MoS_2 and PbS were calculated based on the density functional theory (DFT) in the previous literature, indicating that the adsorption energy of NO_2 on the PbS is significantly larger than that on MoS_2 [52]. Therefore, PbS QDs may serve as receptors of NO_2 molecules and enhance the receptor function of the MoS_2 sensors.
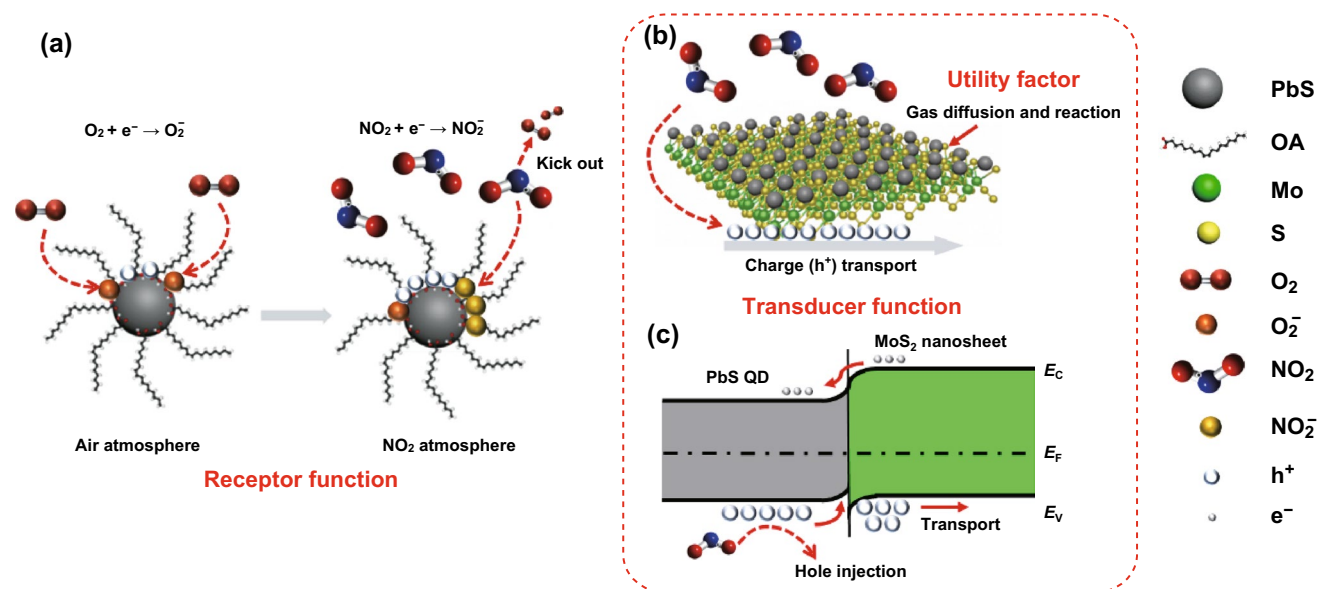

Fig. 6 Schematic illustration of the NO_2-sensing mechanism of MoS_2 nanosheets sensitized with QDs. **a** Receptor function of PbS QDs. **b** Transducer function of MoS_2 nanosheets and the utility factor involved for the sensitized MoS_2 nanosheets. **c** Interface band structure of PbS QD-MoS_2 nanosheet

Combining with Fig. 6b, we also used an interface energy band diagram to further study the sensing mechanism. To simulate the actual environment, Kelvin probe measurement was carried out in ambient air. The work function (W_F) of the PbS QD and MoS$_2$ nanosheet was approximately 4.61 and 4.96 eV, respectively. Next, we used ultraviolet photoelectron spectroscopy (UPS) to confirm the valence-band edge (E_v) [53] and the scan of the spectra for both as shown in Fig. S10. The E_v value was calculated to be 5.20 and 5.46 eV for the PbS QD and MoS$_2$ nanosheet, respectively. We also introduced a UV–Vis–NIR absorption spectrum mainly to evaluate the energy bandgaps (E_g) of the MoS$_2$ nanosheet and PbS QD. As shown in the MoS$_2$ spectrum in Fig. S11a, the characteristic absorption peaks that appeared in the visible regions were consistent with the general features of TMDs with trigonal prismatic coordination, which confirmed the 2H polytype of the MoS$_2$ nanosheet [54]. The intercept was interpolated inside giving the value to E_g of 1.50 eV for MoS$_2$ through the Kubelka–Munk transformed reflectance spectra, indicating that the prepared MoS$_2$ with few-layer nanosheets possesses a bandgap larger than the bulk materials. Figure S11b shows that an exciton absorption peak appeared in 992 nm, from which we could obtain the calculated E_g of 1.25 eV of PbS QD. It exhibited a significantly broadened bandgap compared to the bulk PbS (0.41 eV), confirming a conservation of strong quantum confinement effect [55]. Taking together the above experimental parameters, the initial condition (before mutual contact) of the energy band structure for PbS QD and MoS$_2$ nanosheet could be illustrated in Fig. S12. Because of the difference in work functions (4.61 vs. 4.96 eV), when the PbS and the MoS$_2$ were brought into contact, the electrons pass from the PbS to MoS$_2$, creating a positive charge region closed to the PbS surface and opposite one near the MoS$_2$ surface. Finally, interface band structure was developed for both sides as band bending occurred and a potential barrier of 0.35 eV $\left(\varphi_F = W_{F(PbS)} - W_{F(MoS_2)} \right)$ formed in the contact position, which was accompanied by the balanced E_F. As exhibited in the diagram in Fig. 6c, a majority of the NO$_2$ molecules adsorbed on the surface of the QD receptors may form donor-like surface states in general, and a direct electron extraction from the conduction band of QD into the NO$_2$ molecules, which also meant hole injection from the NO$_2$ into the valence band of QD. Anyway, a mass of holes will accumulate at the interface closed to the side of the PbS QDs during its receptor function process. Equally important

was that the MoS$_2$ nanosheets served as the conductive path in the system, leading the NO$_2$-induced holes flow to the electrode for collection, easily overcoming the relatively low potential barrier generated at the interface of the valence-band edge. DFT calculation results recently demonstrated that the diffusion barrier is only dozens of meV for NO$_2$ on MoS$_2$, which also proved that NO$_2$ gas molecules may easily diffuse rapidly on MoS$_2$ surface [40]. Thus, MoS$_2$ nanosheets can serve as the charge transport highway for the effective transducer function of the sensitized surface adsorption of NO$_2$ gas molecules into an electrical resistance change of the sensor.

Concluded from the above discussion, the sensitized MoS$_2$ sensor had a good response and recovery kinetics even at room temperature because of the favorable 0D QD-2D MoS$_2$ interface, combining the improvement of both receptor function and transducer function [49, 51, 56]. Beyond that, the utility factor is one of the important factors which concerns the gas-sensing performance and goes up with the smaller pore size as well as thinner gas-sensitive film [49]. We took characterization about SEM cross-section morphology of the sensitized MoS$_2$ based on alumina ceramic substrate. However, it was difficult to observe the thickness of such nanothin film clearly on the rough ceramic substrate because it was hard for cutting. Hence, we employed the comparative smooth silicon substrate for material deposition. Figure S13a displays the cross section of the three-layer QD-sensitized MoS$_2$ thin film on silicon substrate, revealing a conformal film deposition, and the film thickness was estimated to be 135 nm. Thus, the utility factor could be benefited greatly from the relatively porous thin-film features, which enhanced the accessibility of inner sulfide grains to the NO$_2$ molecules, leading to enhanced gas diffusion and reaction, thereby achieving higher response along with shorter response/recovery time. We further provided more details in Fig. S13b about NO$_2$-sensing performance of different deposited layers and finally found that the three-layer thin-film-based sensors had a stable response together with a fast recovery time. In brief, our sensitized MoS$_2$ gas sensors exhibited a better NO$_2$ gas-sensing performance at room temperature than that of the pristine MoS$_2$ sensors. The sensitized MoS$_2$ architecture overcome the receptor–transducer function conflict limitation, as well as enhanced the utility factor by sensitizing MoS$_2$ nanosheets with QDs. More importantly, a deeper understanding of the 0D-QDs

with tunable bandgaps will further promote progress in the engineering of energy band alignment at the 0D-2D heterojunction interface, paving a promising way to develop gas-sensing performance of 2D layered materials.

4 Conclusions

In summary, we proposed a facile synthesis strategy for sensitizing MoS_2 nanosheets with PbS quantum dots as NO_2 gas molecules. The sensitized MoS_2 gas sensor exhibited sensitive and recoverable response at room temperature, with the response/recovery time shortened from 50/233 to 15/62 s upon 10 ppm of NO_2 exposure/release cycle, respectively, compared to the pristine MoS_2 nanosheets. The gas-sensing mechanism was attributed to the fundamental factors of receptor function, transducer function and utility, as well as the favorable 0D-2D interface between QDs and MoS_2 nanosheets. Through the surface sensitization of MoS_2 nanosheets with PbS QDs as sensitive and selective NO_2 receptors, combined with the favorable charge transfer at interfaces and excellent charge transport, the receptor and transducer function as well as the utility factor were desirable enhanced, thereby achieving the enhanced performance for NO_2 gas sensing. This work demonstrated a novel sensitized MoS_2 gas sensor with superb sensitivity and extremely low power consumption. The solution-processable and room-temperature operable gas sensors could be integrated with silicon-based or even flexible substrates to achieve smart on-chip electronic nose.

5 Supplementary Material

Homemade sensor setup; SEM image of the flowerlike MoS_2 nanosheets; EDS elemental mapping of QD-sensitized MoS_2 nanosheets; XPS characterization of QD-sensitized MoS_2 nanosheets; repeatability curves and transient resistance characteristic of the MoS_2 nanosheets and QD-sensitized MoS_2 nanosheets sensors; sensor response of QD-sensitized MoS_2 with different Pb:Mo; transient relative response of MoS_2 sensors toward different NO_2 concentrations; LOD calculation of MoS_2 nanosheets sensor and QD-sensitized MoS_2 sensor; sensor response at different relative humidity and long-term stability of the QD-sensitized MoS_2 gas sensors; UPS characterization of MoS_2 nanosheets and PbS QDs; UV–Vis–NIR spectra of MoS_2 nanosheets and PbS QDs; the initial energy band structure of PbS QD and MoS_2 nanosheet; SEM cross-section morphology of QD-sensitized MoS_2 thin film; and NO_2-sensing properties of QD-sensitized MoS_2 with different deposition layers.

References

1. *Environmental Protection Agency (EPA)*. https://www.epa.gov/learn-issues/learn-about-air/ for "Air Pollution, 2013" (2013)

2. F. Xian, B. Zong, S. Mao, Metal-organic framework-based sensors for environmental contaminant sensing. Nano-Micro Lett. **10**, 64 (2018). https://doi.org/10.1007/s40820-018-0218-0

3. T. Xu, Y. Pei, Y. Liu, D. Wu, Z. Shi, J. Xu, Y. Tian, X. Li, High-response NO_2 resistive gas sensor based on bilayer MOS_2 grown by a new two-step chemical vapor deposition method. J. Alloys Compd. **725**, 253–259 (2017). https://doi.org/10.1016/j.jallcom.2017.06.105

4. I. Lee, S.J. Choi, K.M. Park, S.S. Lee, S. Choi, I.D. Kim, C.O. Park, The stability, sensitivity and response transients of ZnO, SnO_2 and WO_3 sensors under acetone, toluene and H_2S environments. Sens. Actuators. B **197**, 300–307 (2014). https://doi.org/10.1016/j.snb.2014.02.043

5. Z. Yuan, J. Zhang, F. Meng, Y. Li, R. Li et al., Highly sensitive ammonia sensors based on Ag-decorated WO_3 nanorods. IEEE Trans. Nanotechnol. **17**(6), 1252–1258 (2018). https://doi.org/10.1109/TNANO.2018.2871675

6. S. Zhang, C. Wang, F. Qu, S. Liu, C.T. Lin et al., ZnO nano-flowers modified with RuO_2 for enhancing acetone sensing performance. Nanotechnology **31**(11), 115502 (2019). https://doi.org/10.1088/1361-6528/ab5cd9

7. F. Qu, H. Jiang, M. Yang, Designed formation through a metal organic framework route of $ZnO/ZnCo_2O_4$ hollow core-shell nanocages with enhanced gas sensing properties. Nanoscale **8**(36), 16349–16356 (2016). https://doi.org/10.1039/C6NR05187A

8. Y. Wang, G. Duan, Y. Zhu, H. Zhang, Z. Xu, Z. Dai, W. Cai, Room temperature H_2S gas sensing properties of In_2O_3 micro/nanostructured porous thin film and hydrolyzation-induced enhanced sensing mechanism. Sens. Actuators B **228**, 74–84 (2016). https://doi.org/10.1016/j.snb.2016.01.002

9. F. Meng, H. Zeng, Y. Sun, M. Li, J. Liu, Trimethylamine sensors based on Au-modified hierarchical porous single-crystalline ZnO nanosheets. Sensors **17**, 1478 (2017). https://doi.org/10.3390/s17071478

10. Z. Yuan, J. Zhao, F. Meng, W. Qin, Y. Chen, M. Yang, M. Ibrahimc, Y. Zhao, Sandwich-like composites of double-layer Co_3O_4 and reduced graphene oxide and their sensing properties to volatile organic compounds. J. Alloys Compd. **793**, 24–30 (2019). https://doi.org/10.1016/j.jallcom.2019.03.386

11. Q. He, Z. Zeng, Z. Yin, H. Li, S. Wu, X. Huang, H. Zhang, Fabrication of flexible MOS_2 thin-film transistor arrays for practical gas-sensing applications. Small **8**(19), 2994–2999 (2012). https://doi.org/10.1002/smll.201201224

12. D.J. Late, Y.K. Huang, B. Liu, J. Acharya, S.N. Shirodkar et al., Sensing behavior of atomically thin-layered MoS_2 transistors. ACS Nano **7**(6), 4879–4891 (2013). https://doi.org/10.1021/nn400026u

13. B. Liu, L. Chen, G. Liu, A.N. Abbas, M. Fathi, C. Zhou, High-performance chemical sensing using Schottky-contacted chemical vapor deposition grown monolayer MoS_2 transistors. ACS Nano **8**(5), 5304–5314 (2014). https://doi.org/10.1021/nn5015215

14. Y. Kim, S.K. Kang, N.C. Oh, H.D. Lee, S.M. Lee, J. Park, H. Kim, Improved sensitivity in schottky contacted two-dimensional MoS_2 gas sensor. ACS Appl. Mater. Interfaces **11**(42), 38902–38909 (2019). https://doi.org/10.1021/acsami.9b10861

15. B. Cho, A.R. Kim, Y. Park, J. Yoon, Y.J. Lee et al., Bifunctional sensing characteristics of chemical vapor deposition synthesized atomic-layered MOS_2. ACS Appl. Mater. Interfaces **7**(4), 2952–2959 (2015). https://doi.org/10.1021/am508535x

16. S.Y. Cho, Y. Lee, H.J. Koh, H. Jung, J.S. Kim, H.W. Yoo, J. Kim, H.T. Jung, Superior chemical sensing performance of black phosphorus: comparison with MOS_2 and graphene. Adv. Mater. **28**(32), 7020–7028 (2016). https://doi.org/10.1002/adma.201601167

17. R. Kumar, N. Goel, M. Kumar, High performance NO_2 sensor using MOS_2 nanowires network. Appl. Phys. Lett. **112**(5), 053502 (2018). https://doi.org/10.1063/1.5019296

18. T. Pham, G. Li, E. Bekyarova, M.E. Itkis, A. Mulchandani, MoS_2-based optoelectronic gas sensor with sub-parts-per-billion limit of NO_2 gas detection. ACS Nano **13**(3), 3196–3205 (2019). https://doi.org/10.1021/acsnano.8b08778

19. H. Im, A. Almutairi, S. Kim, M. Sritharan, S. Kim, Y. Yoon, On MoS_2 thin-film transistor design consideration for a NO_2 gas sensor. ACS Sens. **4**(11), 2930–2936 (2019). https://doi.org/10.1021/acssensors.9b01307

20. Y. Kang, S. Pyo, E. Jo, J. Kim, Light-assisted recovery of reacted MoS_2 for reversible NO_2 sensing at room temperature. Nanotechnology **30**(35), 355504 (2019). https://doi.org/10.1088/1361-6528/ab2277

21. A.V. Agrawal, R. Kumar, S. Venkatesan, A. Zakhidov, G. Yang, J. Bao, M. Kumar, M. Kumar, Photoactivated mixed in-plane and edge-enriched p-type MoS_2 flake-based NO_2 sensor working at room temperature. ACS Sens. **3**(5), 998–1004 (2018). https://doi.org/10.1021/acssensors.8b00146

22. S. Cui, Z. Wen, X. Huang, J. Chang, J. Chen, Stabilizing MOS_2 nanosheets through SnO_2 nanocrystal decoration for high-performance gas sensing in air. Small **11**(19), 2305–2313 (2015). https://doi.org/10.1002/smll.201402923

23. Y. Han, D. Huang, Y. Ma, G. He, J. Hu et al., Design of hetero-nanostructures on MOS_2 nanosheets to boost NO_2 room-temperature sensing. ACS Appl. Mater. Interfaces **10**(26), 22640–22649 (2018). https://doi.org/10.1021/acsami.8b05811

24. B. Cho, J. Yoon, S.K. Lim, A.R. Kim, D.H. Kim et al., Chemical sensing of 2D graphene/MOS_2 heterostructure device. ACS Appl. Mater. Interfaces **7**(30), 16775–16780 (2015). https://doi.org/10.1021/acsami.5b04541

25. Z. Wang, T. Zhang, C. Zhao, T. Han, T. Fei, S. Liu, G. Lu, Rational synthesis of molybdenum disulfide nanoparticles decorated reduced graphene oxide hybrids and their application for high-performance NO_2 sensing. Sens. Actuators B **260**, 508–518 (2018). https://doi.org/10.1016/j.snb.2017.12.181

26. M. Ikram, L. Liu, Y. Liu, L. Ma, H. Lv et al., Fabrication and characterization of a high-surface area MoS_2@WS_2 heterojunction for the ultra-sensitive NO_2 detection at room temperature. J. Mater. Chem. A **7**(24), 14602–14612 (2019). https://doi.org/10.1039/C9TA03452H

27. H.S. Hong, N.H. Phuong, N.T. Huong, N.H. Nam, N.T. Hue, Highly sensitive and low detection limit of resistive NO_2 gas sensor based on a MoS_2/graphene two-dimensional heterostructures. Appl. Surf. Sci. **492**, 449–454 (2019). https://doi.org/10.1016/j.apsusc.2019.06.230

28. T. Chen, W. Yan, J. Xu, J. Li, G. Zhang, D. Ho, Highly sensitive and selective NO_2 sensor based on 3D MoS_2/rGO composites prepared by a low temperature self-assembly method. J. Alloys Compd. **793**, 541–551 (2019). https://doi.org/10.1016/j.jallcom.2019.04.126

29. M. Yuan, M. Liu, E.H. Sargent, Colloidal quantum dot solids for solution-processed solar cells. Nat. Energy **1**(3), 16016 (2016). https://doi.org/10.1038/nenergy.2016.16

30. V. Sukhovatkin, S. Hinds, L. Brzozowski, E.H. Sargent, Colloidal quantum-dot photodetectors exploiting multiexciton generation. Science **324**(5934), 1542–1544 (2009). https://doi.org/10.1126/science.1173812

31. X. Dai, Z. Zhang, Y. Jin, Y. Niu, H. Cao et al., Solution-processed, high-performance light-emitting diodes based on quantum dots. Nature **515**(7525), 96–99 (2014). https://doi.org/10.1038/nature13829

32. H. Liu, M. Li, O. Voznyy, L. Hu, Q. Fu et al., Physically flexible, rapid-response gas sensor based on colloidal quantum dot solids. Adv. Mater. **26**(17), 2718–2724 (2014). https://doi.org/10.1002/adma.201304366

33. H. Liu, S. Xu, M. Li, G. Shao, H. Song et al., Chemiresistive gas sensors employing solution-processed metal oxide quantum dot films. Appl. Phys. Lett. **105**(16), 163104 (2014). https://doi.org/10.1063/1.4900405

34. M. Li, W. Zhang, G. Shao, H. Kan, Z. Song et al., Sensitive NO₂ gas sensors employing spray-coated colloidal quantum dots. Thin Solid Films **618**, 271–276 (2016). https://doi.org/10.1016/j.tsf.2016.08.023

35. Z. Song, Z. Huang, J. Liu, Z. Hu, J. Zhang et al., Fully stretchable and humidity-resistant quantum dot gas sensors. ACS Sens. **3**(5), 1048–1055 (2018). https://doi.org/10.1021/acssensors.8b00263

36. J. Xie, H. Zhang, S. Li, R. Wang, X. Sun et al., Defect-rich MoS₂ ultrathin nanosheets with additional active edge sites for enhanced electrocatalytic hydrogen evolution. Adv. Mater. **25**(40), 5807–5813 (2013). https://doi.org/10.1002/adma.201302685

37. C.B. Murray, D.J. Norris, M.G. Bawendi, Synthesis and characterization of nearly monodisperse CdE (E = sulfur, selenium, tellurium) semiconductor nanocrystallites. J. Am. Chem. Soc. **115**(19), 8706–8715 (1993). https://doi.org/10.1021/ja00072a025

38. S.G. Kwon, Y. Piao, J. Park, S. Angappane, Y. Jo, N.-M. Hwang, J.-G. Park, T. Hyeon, Kinetics of monodisperse iron oxide nanocrystal formation by "heating-up" process. J. Am. Chem. Soc. **129**(41), 12571–12584 (2007). https://doi.org/10.1021/ja074633q

39. J. Zhang, J. Gao, E.M. Miller, J.M. Luther, M.C. Beard, Diffusion-controlled synthesis of Pbs and PbSe quantum dots with in situ halide passivation for quantum dot solar cells. ACS Nano **8**(1), 614–622 (2013). https://doi.org/10.1021/nn405236k

40. X. Xin, Y. Zhang, X. Guan, J. Cao, W. Li, X. Long, X. Tan, Enhanced performances of PbS quantum-dots-modified MoS₂ composite for NO₂ detection at room temperature. ACS Appl. Mater. Interfaces **11**(9), 9438–9447 (2019). https://doi.org/10.1021/acsami.8b20984

41. D. Wang, J.K. Baral, H. Zhao, B.A. Gonfa, V.-V. Truong, M.A. El Khakani, R. Izquierdo, D. Ma, Controlled fabrication of PbS quantum-dot/carbon-nanotube nanoarchitecture and its significant contribution to near-infrared photon-to-current conversion. Adv. Funct. Mater. **21**(21), 4010–4018 (2011). https://doi.org/10.1002/adfm.201100824

42. R.J. Chen, S. Bangsaruntip, K.A. Drouvalakis, N.W. Kam, M. Shim et al., Noncovalent functionalization of carbon nanotubes for highly specific electronic biosensors. Proc. Natl. Acad. Sci. U.S.A. **100**(9), 4984–4989 (2003). https://doi.org/10.1073/pnas.0837064100

43. H. Nan, Z. Wang, W. Wang, Z. Liang, Y. Lu et al., Strong photoluminescence enhancement of MoS₂ through defect engineering and oxygen bonding. ACS Nano **8**(6), 5738–5745 (2014). https://doi.org/10.1021/nn500532f

44. N. Barsan, U. Weimar, Conduction model of metal oxide gas sensors. J. Electroceram. **7**(3), 143–167 (2011). https://doi.org/10.1023/A:1014405811371

45. H. Kan, M. Li, Z. Song, S. Liu, B. Zhang et al., Highly sensitive response of solution-processed bismuth sulfide nanobelts for room-temperature nitrogen dioxide detection. J. Colloid Interfaces Sci. **506**, 102–110 (2017). https://doi.org/10.1016/j.jcis.2017.07.012

46. J. Wu, S. Feng, X. Wei, J. Shen, W. Lu et al., Facile synthesis of 3D graphene flowers for ultrasensitive and highly reversible gas sensing. Adv. Funct. Mater. **26**(41), 7462–7469 (2016). https://doi.org/10.1002/adfm.201603598

47. M. Ridene, I. Iezhokin, P. Offermansand, C.F.J. Flipse, Enhanced sensitivity of epitaxial graphene to NO₂ by water coadsorption. J. Phys. Chem. C **120**(34), 19107–19112 (2016). https://doi.org/10.1021/acs.jpcc.6b03495

48. R. Kumar, N. Goel, M. Kumar, UV-activated MOS₂ based fast and reversible NO₂ sensor at room temperature. ACS Sens. **2**(11), 1744–1752 (2017). https://doi.org/10.1021/acssensors.7b00731

49. N. Yamazoe, Toward innovations of gas sensor technology. Sens. Actuatators B **108**, 2–14 (2005). https://doi.org/10.1016/j.snb.2004.12.075

50. H. Long, A.H. Trochimczyk, T. Pham, Z. Tang, T. Shi et al., High surface area MoS₂/graphene hybrid aerogel for ultrasensitive NO₂ detection. Adv. Funct. Mater. **26**(28), 5158–5165 (2016). https://doi.org/10.1002/adfm.201601562

51. N. Yamazoe, New approaches for improving semiconductor gas sensors. Sens. Actuatators B **128**, 566–573 (1991). https://doi.org/10.1016/0925-4005(91)80213-4

52. X. Zhang, L. Yu, X. Wu, W. Hu, Experimental sensing and density functional theory study of H₂S and SOF₂ adsorption on Au-modified graphene. Adv. Sci. **2**(11), 1500101 (2015). https://doi.org/10.1002/advs.201500101

53. J. Embden, K. Latham, N.W. Duffy, Y. Tachibana, Near-infrared absorbing Cu₁₂Sb₄S₁₃ and Cu₃SbS₄ nanocrystals: synthesis, characterization, and photoelectrochemistry. J. Am. Chem. Soc. **135**(31), 11562–11571 (2013). https://doi.org/10.1021/ja402702x

54. K. Wang, J. Wang, J. Fan, M. Lotya, A. O'Neill et al., Ultrafast saturable absorption of two-dimensional MoS₂ nanosheets. ACS Nano **7**(10), 9260–9267 (2013). https://doi.org/10.1021/nn403886t

55. F.W. Wise, Lead salt quantum dots: the limit of strong quantum confinement. Acc. Chem. Res. **33**(11), 773–780 (2000). https://doi.org/10.1021/ar970220q

56. N. Yamazoe, K. Shimanoe, Basic approach to the transducer function of oxide semiconductor gas sensors. Sens. Actuatators B **160**, 1352–1362 (2011). https://doi.org/10.1016/j.snb.2011.09.075